PAPER

Effect of radial advection on autocatalytic reaction–diffusion fronts

Alessandro Comolli, [ID] L. Negrojević, [ID] Fabian Brau [ID] and A. De Wit [ID] *

The reaction–diffusion–advection properties of autocatalytic fronts are studied both theoretically and experimentally in the case where the autocatalytic species is injected radially into the reactant at a constant flow rate. The theoretical part analyzes both polar and spherical cases. At long times or equivalently large radius from the injection point, the well-known properties of one-dimensional reaction–diffusion autocatalytic fronts are logically recovered as the influence of the advection field decreases radially. At earlier times however, the radial advection impacts the dynamics of the front. We characterize numerically the influence in this transient regime of the injection flow rate and of the ratio of initial concentration of reactant and autocatalytic product on the position of the front, the reaction rate and the amount of product generated. We confirm experimentally the theoretical predictions in polar geometries using the autocatalytic chlorite–tetrathionate reaction.

I. Introduction

Reaction–diffusion (RD) fronts describe a wide variety of processes in natural and engineered systems. Indeed, depending on the nature of the reactants and on the interpretation of the reaction scheme, RD fronts are observed in geochemistry,[1] biology,[2] atmospheric chemistry,[3] and finance,[4] to name a few. Autocatalytic fronts, in which one of the reactants catalyses its own production, represent an important subset of RD fronts, described in very diverse dynamics, including the spreading of infectious agents within the brain,[5] the propagation of flames,[6] or polymerization fronts,[7] for instance.

RD autocatalytic fronts have been thoroughly studied in one-dimensional systems.[8,9] In two-dimensional rectilinear systems, they typically propagate as a reactive planar line along which the autocatalytic species steadily invades the reactants.[10,11] The transverse symmetry of such 2D rectilinear fronts can be broken, giving rise to the formation of lateral instabilities when the reactant diffuses sufficiently faster than the autocatalytic species.[12] Traveling modulated cellular fronts are then observed, as shown both numerically[6] and experimentally.[13,14]

In the presence of flows, oscillating reactions can feature complex dynamics.[15–20] For rectilinear autocatalytic fronts, the influence of advection is trivial when the velocity field is uniform and independent of time, since the problem is then equivalent to the purely diffusive case in a proper co-moving reference frame. Non-uniform flow fields like Poiseuille,[21,22] shear or cellular[23]

Université Libre de Bruxelles (ULB), Nonlinear Physical Chemistry Unit, CP231,
1050 Bruxelles, Belgium. E-mail: anne.de.wit@ulb.be

and pulsatile[24] flow fields are however known to modify the dynamics of autocatalytic fronts.

In parallel, the effect of geometry on the dynamics and transverse instability of RD autocatalytic fronts has also been investigated,[25] by considering axisymmetric and spherical RD fronts, in which the autocatalytic species invades the reactants radially in 2D or 3D, respectively. For sufficiently long times or large radius *i.e.* when the advection velocity tends to zero, the travelling fronts progress in the radial direction with the same speed as for 1D RD rectilinear fronts.

In such radial geometries, advection plays however a crucial role at earlier times *i.e.* small radius when the velocity field is not uniform and constant. For simple bimolecular A + B → C fronts, it has been shown that radial advection can control the propagation speed, reaction rate and amount of product generated in time.[26–33] The impact of radial advection on autocatalytic fronts remains however not characterized.

In this framework, we study here theoretically and experimentally to what extent the dynamics of autocatalytic fronts is affected by radial advection when the autocatalytic species is injected radially into the reactant at a constant flow rate. To this end, we analyze analytically and numerically the dynamics of reaction–diffusion–advection (RDA) fronts using a cubic autocatalytic scheme of the kind

$$2X + Y \rightarrow 3X, \tag{1}$$

where X is the autocatalytic species and Y the reactant. We compute numerically the temporal evolution of the position of the front, of the reaction rate, and of the amount of product generated for both axisymmetric and spherical geometries in presence of radial advection. At asymptotic long times or

equivalently large radius, we recover the properties of the rectilinear 1D fronts because the influence of the advective field decreases inversely to the radius. We characterize the influence of varying the flow rate and the initial ratio of concentrations of the reactant and autocatalytic species on the transient dynamics. We confirm the theoretical predictions experimentally by studying the dynamics of an autocatalytic chlorite–tetrathionate (CT) front[34,35] in a confined axisymmetric geometry with radial injection.

This paper is structured as follows. Section II introduces the reaction and transport model in both polar and spherical geometries and defines the observables used to characterize the dynamics of RDA fronts. In Sections III and IV, we derive analytical predictions for the early and long-time dynamics of polar and spherical fronts, respectively, and we compare them with numerical results. For polar fronts, we additionally present experimental results that validate the theoretical study. Section V discusses the impact of geometry. Finally, Section VI summarizes the main results and concludes the paper.

II. RDA model

We consider a system where the autocatalytic species X in initial concentration $\bar{x}_0$ is injected radially into the reactant Y in initial concentration $\bar{y}_0$. The dimensional concentrations of X and Y are indicated by $\bar{x}$ and $\bar{y}$, respectively. Both species undergo passive advection and molecular diffusion. Upon contact between the reactants, the cubic autocatalytic reaction (1) takes place, and the RDA equations describing the dynamics of the system are

$$\partial_{\bar{t}}\bar{x} + \bar{\mathbf{v}} \cdot \bar{\nabla}\bar{x} = \bar{D}_X\bar{\nabla}^2\bar{x} + k\bar{x}^2\bar{y}, \tag{2a}$$

$$\partial_{\bar{t}}\bar{y} + \bar{\mathbf{v}} \cdot \bar{\nabla}\bar{y} = \bar{D}_Y\bar{\nabla}^2\bar{y} - k\bar{x}^2\bar{y}, \tag{2b}$$

where $\bar{t}$ is the dimensional time, $\bar{D}_X$ and $\bar{D}_Y$ are the diffusion coefficients of the corresponding species and k is the reaction kinetic constant. In this study, we will assume flow incompressibility $\bar{\nabla} \cdot \mathbf{v} = 0$ and that both species have the same diffusivity, namely $\bar{D}_X = \bar{D}_Y = \bar{D}$.

Note that autocatalytic fronts can become unstable transversally because of a diffusive instability occurring when the reactant Y diffuses sufficiently faster than the autocatalytic species X.[6] Experimentally, this is typically achieved by loading gels with a complexing agent of high molecular mass, that binds to X.[13,14] In the present case, the experiments are done in aqueous solutions with no complexing agent while our assumption that $\bar{D}_Y = \bar{D}_X$ in the modelling ensures that no diffusive instability is present. Another possibility would be to destabilize the front because of buoyancy-driven convection[36,37] or viscous fingering.[15] No hydrodynamic instability is taken into account into the modelling while no such instabilities are observed experimentally, the density and viscosity of both reactant and product aqueous solutions being very similar. In absence of any transverse deformation, we have thus radial symmetry, *i.e.* the velocity flow field is oriented radially and its

intensity only depends on r so that $\bar{\mathbf{v}} = \bar{v}_r(\bar{r})\mathbf{e}_r$, where $\mathbf{e}_r$ is the unit vector aligned with the radial direction r.

A. Polar geometry

In polar geometry, the conditions of flow incompressibility and radial symmetry imply that the intensity of velocity is

$$\bar{v}_r = \frac{\bar{Q}}{2\pi\bar{h}\bar{r}}, \tag{3}$$

where $\bar{Q}$ is the flow rate and $\bar{h}$ is the reactor thickness. Eqn (2) are expressed in dimensionless units by rescaling times by the chemical time $\bar{\tau} = 1/k\bar{y}_0^2$, lengths by $\bar{\ell} = \sqrt{\bar{D}\bar{\tau}}$ and concentrations by $\bar{y}_0$. They read

$$\partial_t x(r,t) + \frac{Q-1}{r}\partial_r x(r,t) = \partial_r^2 x(r,t) + R(r,t) \tag{4a}$$

$$\partial_t y(r,t) + \frac{Q-1}{r}\partial_r y(r,t) = \partial_r^2 y(r,t) - R(r,t), \tag{4b}$$

where the dimensionless flow velocity and flow rate are

$$v_r = \frac{Q}{r}, \quad Q = \frac{\bar{Q}}{2\pi\bar{h}\bar{D}}, \tag{5}$$

and $R = x^2y$ is the reaction rate. We solve the coupled partial differential equations (PDE) (4) with the initial conditions $x(r,0) = \gamma H(-r)$ and $y(r,0) = H(r)$, where

$$\gamma = \frac{\bar{x}_0}{\bar{y}_0} \tag{6}$$

is the ratio between the initial concentrations of the injected autocatalytic species X and of the displaced reactant Y, $H(\cdot)$ is the Heaviside function, and the boundary conditions are $x(r \to 0,t) = \gamma$, $x(r \to \infty,t) = y(r \to 0,t) = 0$ and $y(r \to \infty,t) = 1$. In Appendix A, we show how to decouple the PDEs, which is useful for computational purposes. In the numerical simulations, the boundary conditions at infinity are imposed at the outer radius R of the numerical domain, with R typically twice the largest value of the front position, such that it does not affect the measured scalings. As an example, for $Q = 10$, R was equal to 15 000 units of length.

B. Spherical geometry

In spherical geometry, the injection flow velocity is given by

$$\bar{v}_r = \frac{\bar{Q}}{4\pi\bar{r}^2}. \tag{7}$$

Nondimensionalization is carried out as in the previous section. Since the radial part of the Laplacian in spherical coordinates reads $\nabla^2 = 2/r\partial_r + \partial_r^2$, eqn (2) reduce to the following set of governing equations

$$\partial_t x(r,t) + \left(\frac{Q}{r^2} - \frac{2}{r}\right)\partial_r x(r,t) = \partial_r^2 x(r,t) + R(r,t) \tag{8a}$$

$$\partial_t y(r,t) + \left(\frac{Q}{r^2} - \frac{2}{r}\right)\partial_r y(r,t) = \partial_r^2 y(r,t) - R(r,t), \tag{8b}$$

This journal is © the Owner Societies 2023

Phys. Chem. Chem. Phys., 2023, **25**, 10604–10619 | **10605**

where

$$v_r = \frac{Q}{r^2}, \quad Q = \frac{\bar{Q}}{4\pi \bar{D}^{3/2}\tau^{1/2}}. \tag{9}$$

The boundary and initial conditions are the same as in the polar geometry.

C. Observables

We carry out the description of autocatalytic fronts by studying the temporal evolution of some observables characterizing the front properties. First, we consider the front position r_f, which is defined here as the distance from the inlet at which the concentrations of X and Y are equal, *i.e.* $x(r_f) = y(r_f)$. The intensity of the reaction is quantified in terms of the maximum reaction rate $R^{max}(t) = \max_r R(r,t)$. The position r_{max} where the production rate is maximum and r_f are not necessarily equal and represent two complementary ways to describe the front motion. The front extension is quantified through the width w of the production rate, which is computed as the width at half-height of $R(r,t)$. Finally, we analyze the temporal evolution of the total amount n_x of the autocatalytic species X, which is obtained through the integration of the concentration x in the whole domain Ω

$$n_x(t) = \int_\Omega x(r,t)\mathrm{d}\mathbf{r}, \quad \bar{n}_x(\bar{t}) = \bar{y}_0\bar{\ell}^3 n_x. \tag{10}$$

The amount of product in polar geometry n_x^{POL} and in spherical geometry n_x^{SPH} are derived by properly expressing the integration in eqn (10) as

$$n_x^{POL}(t) = 2\pi h \int_0^\infty r x(r,t)\mathrm{d}r \tag{11a}$$

$$n_x^{SPH}(t) = 4\pi \int_0^\infty r^2 x(r,t)\mathrm{d}r. \tag{11b}$$

III. Polar fronts

Let us start by studying the dynamics of autocatalytic fronts in polar geometry. First, we present in Section IIIA the theoretical results for the early- and long-time RDA limits in the presence of advection, and compare them to the full temporal dynamics obtained through numerical computations. Then, a validation of the theory with experimental results is presented in Section IIIB.

A. Theory of polar autocatalytic fronts

The theoretical RDA model describing the evolution of polar autocatalytic fronts is given by eqn (4) along with the given initial and boundary conditions. Let us discuss the solution to these equations in the early and long time regimes.

1. Early-time regime. As observed in earlier works on A + B → C fronts,[28,31] when the two reactants start to be in contact the amount of mixing at early times is small and the influence of reaction is negligible. Thus, analytical solutions for the early-time concentration profiles x_E and y_E can be obtained by neglecting the reaction term in eqn (4) (see Appendix B1).
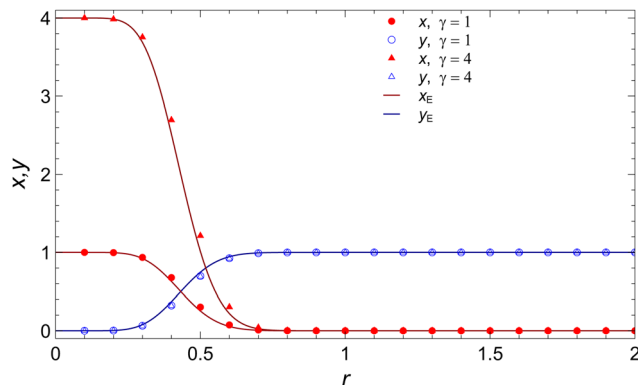

Fig. 1 Early-time radial concentration profiles at $t = 10^{-2}$ for $Q = 10$ and $\gamma = 1$ or $\gamma = 4$ for polar fronts. The symbols represent the numerical solutions, while the solid curves represent the analytical solutions (12).

They read

$$x_E(r,t) = \gamma \mathcal{Q}\left(\frac{Q}{2}, \frac{r^2}{4t}\right), \tag{12a}$$

$$y_E(r,t) = 1 - \mathcal{Q}\left(\frac{Q}{2}, \frac{r^2}{4t}\right) = 1 - \frac{x_E(r,t)}{\gamma}, \tag{12b}$$

where $\mathcal{Q}(\alpha,\cdot) = \Gamma(\alpha,\cdot)/\Gamma(\alpha)$, $\Gamma(\alpha,\cdot)$ and $\Gamma(\alpha)$ are the regularized, incomplete and complete gamma functions, respectively.[38] Fig. 1 shows good agreement between the approximated solutions (12) and the results of numerical computations of eqn (4).

The early-time front position $r_{f,E}$ is obtained by equating x_E and y_E, given by eqn (12), which yields $x_E = y_E = \gamma/(1 + \gamma)$ and, from eqn (12a),

$$r_{f,E}(t) = 2\sqrt{\mathcal{K}_E t}, \quad \bar{r}_{f,E}(\bar{t}) = 2\sqrt{\mathcal{K}_E \bar{D}\bar{t}}, \tag{13a}$$

$$\mathcal{K}_E(Q,\gamma) = \mathcal{Q}^{-1}\left(\frac{Q}{2}, \frac{1}{1+\gamma}\right). \tag{13b}$$

Fig. 2a shows good agreement between eqn (13a) and the early-time temporal evolution of r_f obtained through numerical computations for different values of flow rate Q and ratio of initial concentrations γ. Notice that, at early times, the autocatalytic front moves as the long-time asymptotic A + B → C RDA front in polar geometry,[26] once we account for the correspondence $\gamma \leftrightarrow 1/\gamma$ between the two articles. This means that, in these regimes, the motion of the front is governed by volume conservation, independently of the kinetics. In fact, because the amount of mixing between the reactants is small at early times, we can neglect the contribution of reaction and thus the conservative component $u = x - y$ satisfies the same equation with the same boundary conditions as for A + B → C RDA polar fronts. Fig. 2a shows that, for $Q = 10$, varying the ratio γ of initial concentrations of the reactants impacts the dynamics of front. The front velocity is larger when the injected species is in a larger initial concentration than the invaded species ($\gamma > 1$) and smaller when $\gamma < 1$. However, for $Q \gg 1$, we have $K_E \sim Q/2$,[26] so that the front position no longer depends on γ. This effect is
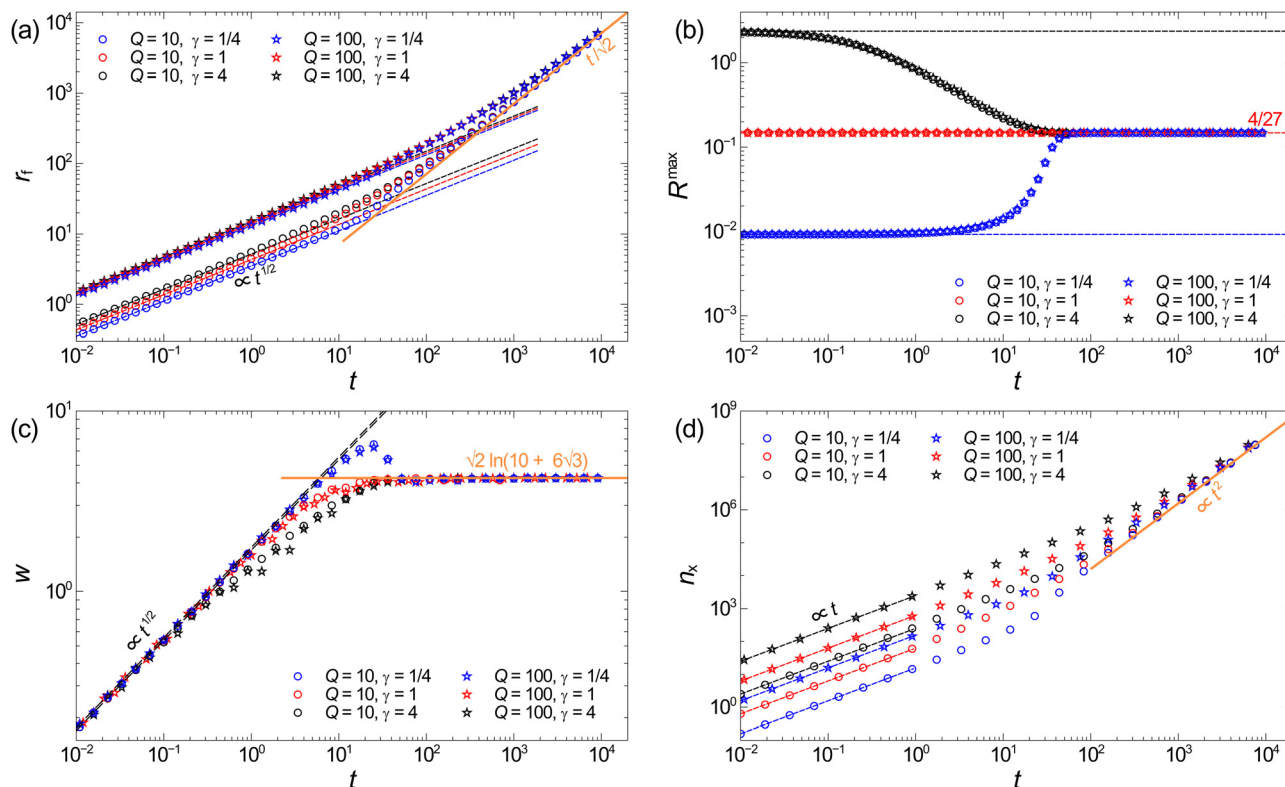
Fig. 2 Temporal evolution of the observables for polar fronts, obtained by solving numerically eqn (4) together with analytical asymptotic scalings. (a) Front position r_f. The dashed lines represent the early-time $\sim t^{1/2}$ dependence given by eqn (13a), while the solid orange line represents the long-time asymptotic $t/\sqrt{2}$ regime (23). (b) Maximum production rate. The dashed lines represent the early value $4\gamma^2/27$ given by eqn (15). Notice that, for $\gamma = 1$, the early-time and the long-time asymptotic trend $4/27$ given by eqn (24) are equal. (c) Front width. The orange solid line represents $w_A \sim 4.26$ (eqn (25)), while the black dashed lines represent $w_E \simeq 2\Theta(Q)t^{1/2}$ (eqn (17)). (d) Total amount of autocatalytic species. At early times, n_x grows linearly with time, as shown by the dashed lines (eqn (19)), while the orange line represents the long-time ballistic $\sim t^2$ growth given by eqn (26).

already seen in Fig. 2a at $Q = 100$, where changing γ by a factor 16 has a little impact on the front position.

At early times, the following expression for the production rate $R_E = x_E^2 y_E$ becomes, using eqn (12b),

$$R_E(r, t) = x_E^2(r, t)\left(1 - \frac{x_E(r, t)}{\gamma}\right), \qquad (14)$$

where x_E is given by eqn (12a). The temporal evolution of its maximum along r is shown in Fig. 2b. In Appendix B1, we show that, at early times, it is

$$R_E^{max} = \frac{4\gamma^2}{27}, \quad \bar{R}_E^{max}(\bar{r}, \bar{t}) = \frac{4}{27}\gamma^2 k \bar{y}_0^3. \qquad (15)$$

The production rate is maximum when $x_E = x_E^{max} = 2\gamma/3$, which occurs at the radial position

$$r_E^{max} = 2\sqrt{H_E t}, \quad H_E(Q) = \mathcal{Q}^{-1}\left(\frac{Q}{2}, \frac{2}{3}\right), \qquad (16a)$$

$$\bar{r}_E^{max} = 2\sqrt{H_E \bar{D}\bar{t}}. \qquad (16b)$$

In the limit $Q \gg 1$, we can approximate $H_E \simeq Q/2$ and the position r_E^{max} of the maximum production rate coincides then with the front position $r_{f,E}$. Notice that the maximum production rate (15) is constant at early-times. This behavior was also

observed for $A + B \rightarrow C$ fronts in different radial geometries,[28,31] but with a different constant, namely $\gamma/4$.

The temporal evolution of full width at half height of the production rate is shown in Fig. 2c. The analytical expression of its early-time limit w_E is derived in Appendix B1 and it reads

$$w_E(t) = 2\Theta(Q)t^{1/2}, \quad \bar{w}_E(\bar{t}) = 2\Theta(Q)\sqrt{\bar{D}\bar{t}}, \qquad (17)$$

where

$$\Theta(Q) = \sqrt{\mathcal{Q}^{-1}\left(\frac{Q}{2}, \frac{1}{3}\right)} - \sqrt{\mathcal{Q}^{-1}\left(\frac{Q}{2}, \frac{1 + \sqrt{3}}{3}\right)}. \qquad (18)$$

As we show in Appendix B1, for $Q \gtrsim 5$, $\Theta(Q)$ saturates quickly to the value 0.89. As shown in Fig. 2c, the front width is independent of γ at early times and it increases diffusively as $t^{1/2}$.

At early times, the total amount of the autocatalytic species $n_{x,E}$ is obtained by substituting eqn (12a) into eqn (11a) and, knowing that $\int_0^\infty \mathcal{Q}(Q/2, z)dz = Q/2$, it reads

$$n_{x,E}(t) = 2\pi h\gamma Q t, \quad \bar{n}_{x,E}(\bar{t}) = \bar{x}_0 \bar{V}, \qquad (19)$$

where $\bar{V}$ is the injected volume of X. This shows that the number of molecules in the system is equal to the number of molecules injected, because the contribution of the reaction is negligible at early times. Thus, we see that the presence of
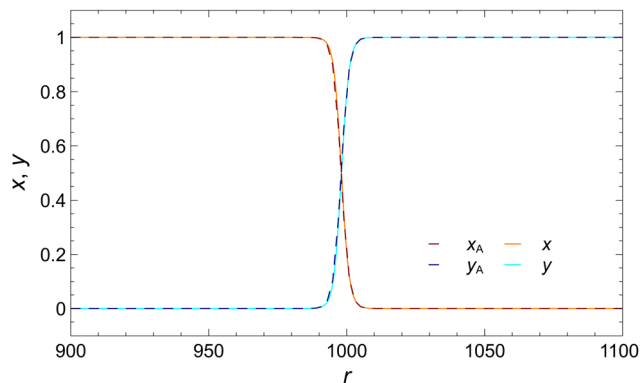
Fig. 3 Concentration profiles at $t = 10^3$ for $Q = 100$ and $\gamma = 1$ for polar fronts, obtained by solving numerically eqn (4). The dashed lines represent the approximated solutions (21) and (22).

advection implies that the amount of product generated increases linearly in time with a slope directly proportional to the flow rate Q (Fig. 2d). If Q is constant and γ is increased, a larger amount of X is present, since the initial concentration of the injected unreacted autocatalytic species is then higher.

2. Long-time regime. In the long-time regime, the evolution of the concentration of the reactant Y is described by the following equation, whose derivation is shown in Appendix C

$$\partial_\xi^2 y_A + c(t)\partial_\xi y_A - (1 - y_A)^2 y_A = 0, \quad (20)$$

where the index A stands for asymptotic long-time, $\xi = r - r_{f,A}(t)$, where $r_{f,A}$ is the front position at late times and $c(t) = dr_{f,A}/dt$ is the front velocity. In agreement with Fig. 2a, we assume that, at long times, the front moves with a constant velocity, as for the rectilinear case, i.e. that $c(t) = c$ is a constant. This ansatz is confirmed *a posteriori* by numerical computations, since the solution of eqn (20) with constant c matches with the long-time solutions of eqn (4b) (see Fig. 3). Hence, eqn (20) reduces to the cubic Fisher equation,[39] whose solution is[25]

$$y_A(r, t) = \frac{1}{1 + \exp\left[-\dfrac{r - r_{f,A}(t)}{\sqrt{2}}\right]}, \quad c = 1/\sqrt{2}. \quad (21)$$

The concentration x_A of the autocatalyst is obtained by using $x_A + y_A = 1$ (see Appendix C) and it reads

$$x_A(r, t) = 1 - y_A(r, t) = \frac{\exp\left[-\dfrac{r - r_{f,A}(t)}{\sqrt{2}}\right]}{1 + \exp\left[-\dfrac{r - r_{f,A}(t)}{\sqrt{2}}\right]}. \quad (22)$$

Notice that the front velocity $c = 1/\sqrt{2}$ at long times is the same as in the purely RD rectilinear[40] and radial cases.[25] This means that, at long times, the contribution of advection to the front dynamics is negligible, as the velocity is fully determined by the autocatalytic reaction and diffusion. Indeed, by advection only, the front position would move with a velocity $\bar{\omega}$ given by volume conservation as $\bar{\omega} = (\bar{Q}/4\pi\bar{h}\bar{t})^{1/2}$. The front velocity $\bar{c}$ at long times is constant and given by $\bar{c} = \bar{\ell}/(\bar{\tau}\sqrt{2})$. Thus, we can define a time scale at which the system is in the long-time regime, which
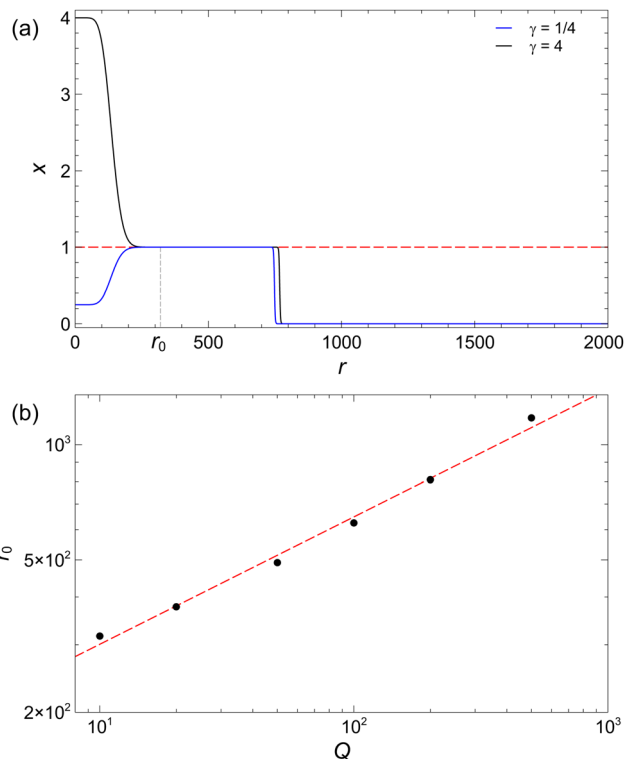

Fig. 4 (a) Concentration profiles of the autocatalytic species X at $t = 10^3$ for $Q = 10$ and two values of γ. (b) Dependence of r_0 on the injection flow rate Q. The dashed line represents $r_0(Q) \simeq 139.6Q^{1/3}$.

occurs when $\bar{c} \gg \bar{\omega}$. This condition holds for $\bar{t} \gg \bar{Q}\bar{\tau}/(2\pi\bar{D}\bar{h})$, which, in dimensionless units, reads $t \gg Q$. Then, the front position at long times is given by the simple linear relationship

$$r_{f,A}(t) = ct = t/\sqrt{2}, \quad \bar{r}_{f,A}(\bar{t}) = \sqrt{\frac{\bar{D}}{2\bar{\tau}}}\bar{t}. \quad (23)$$

The temporal evolution of the front position is shown in Fig. 2a. We see that, for $t \gtrsim 10^3$, all curves converge towards the same relationship (23) whatever the values of Q and γ. In this long-time regime, the front travels at a constant speed with a fixed shape shown in Fig. 3. As a result, the maximum production rate R_A^{max} (Fig. 2b) and the front width w_A (Fig. 2c) also become constants. Their values are calculated in Appendix C and read

$$R_A^{max}(t) = \frac{4}{27}, \quad \bar{R}_A^{max}(\bar{t}) = \frac{4k\bar{y}_0^3}{27} \quad (24)$$

and

$$w_A = \sqrt{2}\ln(10 + 6\sqrt{3}) \simeq 4.26, \quad \bar{w}_A = 4.26\sqrt{\bar{D}\bar{\tau}}. \quad (25)$$

Fig. 2b and c show good agreement between the numerical results and the analytical predictions.

While the observables presented so far for polar fronts exhibit the same behaviors as in rectilinear geometry, the front shape has a strong impact on the temporal evolution of the amount n_x of X generated behind the front. In fact, while for rectilinear fronts the contact surface between the reactant and the autocatalytic species is constant, in polar and spherical
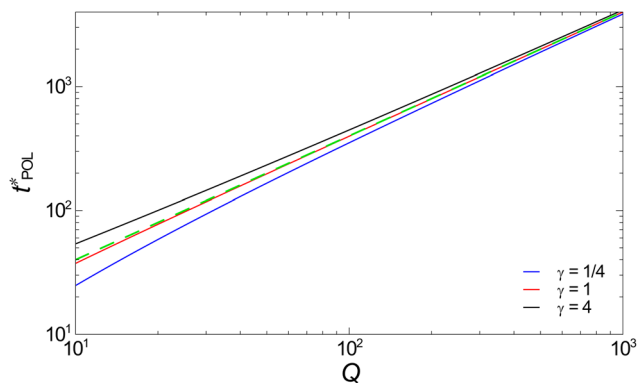
10608 | *Phys. Chem. Chem. Phys.*, 2023, **25**, 10604–10619

This journal is © the Owner Societies 2023

Fig. 5 Transition time between the early-time and the long-time regimes as of eqn (28). The dashed line represents the limit $t^*_{POL} \sim 4Q$ for high flow rates.

geometries this area grows with the expansion of the radial front. The long-time value of n_x in polar geometry, derived in Appendix C, grows ballistically with respect to time

$$n^{POL}_{x,A}(t) \simeq \frac{\pi h}{2}t^2, \quad \bar{n}^{POL}_{x,A}(\bar{t}) \simeq \frac{\bar{D}}{2\bar{\tau}}\pi\bar{y}_0\bar{h}\bar{t}^2, \tag{26}$$

whereas for rectilinear fronts a linear growth is observed

$$n^{RECT}_{x,A}(t) \simeq \frac{hL}{2\sqrt{2}}t, \quad \bar{n}^{RECT}_{x,A}(\bar{t}) \simeq \sqrt{\frac{\bar{D}\bar{h}\bar{L}\bar{y}_0}{2\bar{\tau}}}\frac{\bar{L}\bar{y}_0}{2}\bar{t}, \tag{27}$$

where $L = \bar{L}/\bar{\ell}$ is the dimensionless length of the contact line between the species. Thus, at long times, a much larger amount of X is obtained in the radial geometry compared to the rectilinear one at a given time, as for A + B → C fronts.[29] We observe good agreement between the expression (26) and the numerical solutions for the total amount of X, as shown in Fig. 2d.

To conclude this section, we show that the presence of advection allows to keep $\gamma \neq 1$ over a certain distance from the inlet, as shown in Fig. 4a. In particular, Fig. 4b shows that the distance r_0 at which the autocatalytic reaction resets the concentration of the injected species to 1 depends on the flow rate as $r_0 \simeq 139.6Q^{1/3}$.

3. Transition time. To obtain the transition time t^*_{POL} between the early and the long-time regimes, we require that the early-time and the long-time expressions of the front position r_f should be equal. Thus, by equating the right-hand side terms of eqn (13a) and (23), we obtain for $Q \gg 1$

$$t^*_{POL}(Q,\gamma) = 8\mathcal{K}_E(Q,\gamma), \quad \bar{t}^*_{POL} = 8\mathcal{K}_E(Q,\gamma)\bar{\tau}, \tag{28}$$

with $\mathcal{K}_E$ given by eqn (13b). As $\mathcal{K}_E \sim Q/2$ for $Q \gg 1$, we have in that limit that $t^*_{POL} \sim 4Q$. As shown in Fig. 5, the transition time is essentially independent of γ for large values of the injection flow rate. This can be confirmed by inspecting Fig. 2a, where we see that, indeed, for $Q = 10$, the transition between the advection-dominated regime and the later RD regime occurs around $t \sim 40$. For $Q = 100$, the transition occurs much later and the effect of advection allows the front to travel faster during a longer time. We see also that indeed the effect of varying γ is visible for $Q = 10$ but becomes negligible for $Q = 100$. The dimensionless
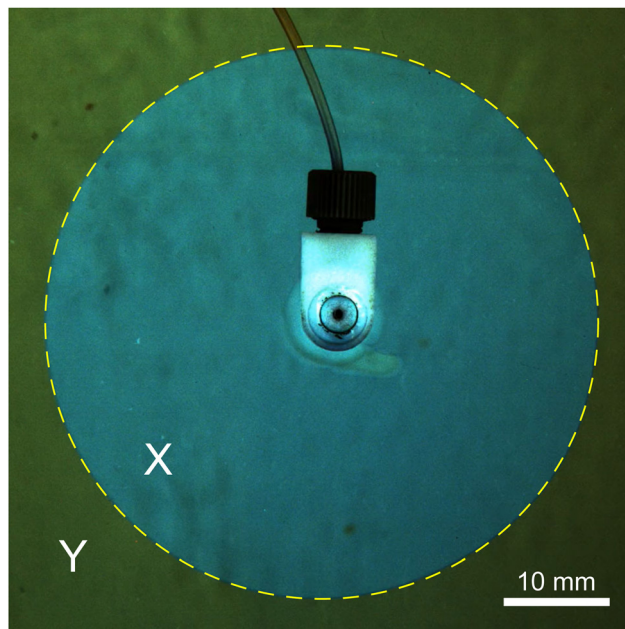

Fig. 6 Experimental results: Snapshot at $\bar{t} = 350$s of the chemical front propagating radially in a Hele-Shaw cell when the autocatalytic species X ([HNO$_3$] = 0.025 M) is injected radially into the reactant solution Y of the chlorite–tetrathionate reaction at a constant flow rate $\bar{Q} = 5$ μL min^{-1}. The dashed circle shows that the front is circular.

flow rate $Q = 10$ corresponds to the dimensional flow rate $\bar{Q} \simeq 3.8 \times 10^{-3}$ mL min^{-1}, if we consider the gap height $\bar{h} = 1$ mm and the diffusion coefficient $\bar{D} = 10^{-9}$ m^2 s^{-1}.

B. Experimental results

To verify the theoretical predictions for polar fronts, we turn to one of the well-known autocatalytic reactions *i.e.* the chlorite–tetrathionate (CT) reaction[41] which has been subject of many experimental studies including autocatalytic front propagation in capillaries,[35] convective instabilities,[42–44] programmable acid autocatalysis,[45] and nanoparticle self-assembly.[46] In the following section, we describe the experimental methodology, and we present the results by comparing them to the analytical predictions.

1. Materials and methods. We prepare the reactant solution, containing 20 mM of sodium chlorite (NaClO$_2$) and 5 mM of potassium tetrathionate (K$_2$S$_4$O$_6$), at room temperature, using the reagents of the highest commercially available degree of purity (Sigma Aldrich). We use 0.5 mM of Congo red or Methyl red indicator to observe the front position. Although not a reactant *per se*, 7 mM of sodium hydroxide is added to the system to prevent the reaction from self-initiating. The auto-catalytic front dynamics are studied in a horizontal Hele-Shaw cell consisting of two glass plates separated by a 0.12 mm gap initially filled with the reactant solution. Nitric acid providing the autocatalytic species X (proton) is injected radially using a syringe pump (KD Scientific Legato 210) into the reactant solution Y at given flow rates (5 to 40 μL min^{-1}) to study the influence of radial advection on the front position. We monitor the temporal evolution of the front position using an IDS UI

This journal is © the Owner Societies 2023

Phys. Chem. Chem. Phys., 2023, **25**, 10604–10619 | **10609**

$\bar{y}_0$	$(5 \pm 1) \times 10^{-3}$ M
$\bar{D}$	$(9.5 \pm 0.1) \times 10^{-9}$ m^2 s^{-1}
k	$(2.71 \pm 0.23) \times 10^3$ s^{-1} M^{-2}
$\bar{\tau}$	(14.9 ± 1.3) s
$\bar{\ell}$	(0.37 ± 0.02) mm

3060CP-C-HQ Rev.2 camera. As seen on Fig. 6, the front is relatively sharp, usually 3–5 pixels wide, corresponding to 0.2 to 0.4 mm. This front width remains constant throughout the experiments. The front position is defined as the location along a radius where the reactant solution's color changes due to the reaction occurring. Except in some experiments where self-initiation at the borders or bubbles affected the propagation, the front propagates usually as a circle as seen on Fig. 6. The measured front position is then obtained as an average of the positions measured along typically three different radii.

  2. Experimental results. In order to analyze the quantitative agreement between the long-time experimental results obtained in Hele-Shaw cells and the theoretical RDA predictions, we solve the equation for the simplified model of the CT reaction.[35] We find the dimensionless front velocity (23) here to be $c^{CT} = 6/\sqrt{2}$, where the factor 6 comes from the specific stoichiometry of the

Fig. 7 Experimental results: temporal evolution of (a and b) the RDA front position for [HNO$_3$] = 0.1 M (γ = 18.6) and different flow rates, and (c and d) the RDA front position for $\bar{Q}$ = 5 μL min^{-1} and $\bar{Q}$ = 10 μL min^{-1} and different concentrations of the initiator. The dashed blue lines indicate the early-time regime (30). The solid lines represent eqn (31), which asymptotically grows with the linear trend $\sim \bar{t}$.

CT reaction.[35] Taking the factor 6 into account in eqn. (21) and (22), we find the reaction front position as the location where $x_A = y_A$:

$$r_{f,A}^{CT} = c^{CT}t + \frac{\ln 6}{c^{CT}} = c^{CT}t + \frac{\sqrt{2}\ln 6}{6} \simeq c^{CT}t + 0.422,$$

$$\bar{r}_{f,A}^{CT} = \bar{\ell}\left[\frac{c^{CT}}{\bar{\tau}}\bar{t} + 0.422\right]. \tag{29}$$

The values of the experimental parameters are listed in Table 1.

  The effect of advection on the experimental front dynamics is presented in Fig. 7a, which shows the temporal evolution of the position of RDA fronts for different flow rates. After a certain period, no matter the value of the flow rate, we should recover the same behavior as in the long-time RD regime. However, on the temporal scale of the experiment, the dynamics have not converged to the long-time asymptotic regime, which explains the difference in slopes observed at longer times on Fig. 7a. Eqn (28) provides an estimate of the transition time from the early-time regime $\sqrt{t}$ to the long-time $\bar{t}$ regime. In the case of a 5 μL min^{-1} flow rate and for the values of parameters given in Table 1, this time equals 867 s. However, already at the end of the experiment, *i.e.* at experimental times of 600 s, we observe that the front position for $\bar{Q}$ = 5 μL min^{-1} evolves almost linearly with time, as $\bar{t}^{(0.95\pm0.01)}$.

  Advection affects the transient regime by suppressing the influence of the initiator's concentration (x_0). As shown in Fig. 7c, with an increase in flow rate, regardless of the acid concentration used to initiate the autocatalytic reaction, RDA fronts evolve in the same way.

  3. Comparison with theory. In order to compare the early-time predictions (13a) with the experimental data, we need to account for some effects. First, as already seen in some experimental works,[26,30] at early times, the injected reactant does not fill the gap completely. Second, the flow at short time is certainly not yet fully developed in the experiments so that its gap averaged expression differs from eqn (3) from which eqn (13a) is derived. We find that these effects can be accounted for by introducing a constant $\bar{c}_1$, whose value is fitted from data, to eqn (13a), which then reads

$$\bar{r}_{f,E}(\bar{t}) = 2\sqrt{\mathcal{K}_E \bar{D}\bar{t}} + \bar{c}_1. \tag{30}$$

In the experiments presented in this section, the long-time regime is generally not reached, due to limitations in the size of the cells. Thus, the front dynamics still conserves a memory of the initial conditions, which are accounted for through an additive constant $\bar{c}_2$ in eqn (29), whose values are obtained through fitting from experimental data. Hence, eqn (29) reads

$$\bar{r}_{f,A}^{CT} = \bar{\ell}\left[\frac{c^{CT}}{\bar{\tau}}\bar{t} + 0.422\right] + \bar{c}_2. \tag{31}$$

Here again, this relation fits the experimental data quite well at later times. This confirms the switch from a diffusive regime at early times to a linear trend later on.
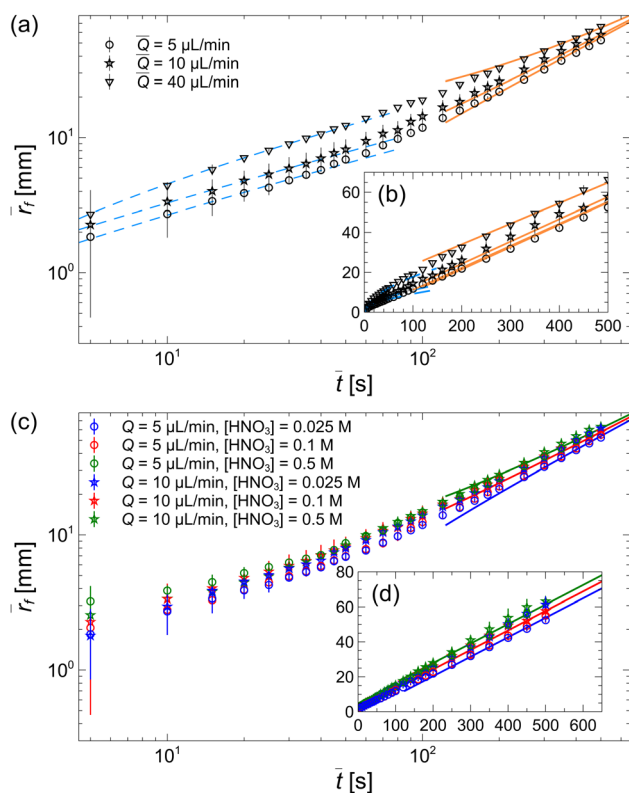
10610 | *Phys. Chem. Chem. Phys.*, 2023, **25**, 10604–10619

This journal is © the Owner Societies 2023

IV. Spherical fronts

In this section, we study the dynamics of spherical RDA autocatalytic fronts, which is governed by eqn (8). Due to the complexity of experiments in spherical geometry, here we only provide the theoretical analysis. Experimental validation of the theory is left to future studies.

A. Early-time regime

As we did for polar fronts, we assume here that the amount of mixing between the two species X and Y is small at early times, hence we neglect the reaction terms in eqn (8). In Appendix B2, we derive the following asymptotic solutions accounting for only advection and diffusion

$$x_E(r, t) = \frac{\gamma}{2}\left[1 - \text{erf}\left(\sqrt{\frac{7}{12}}\frac{r - r_f^{ad}(t)}{\sqrt{t}}\right)\right], \qquad (32a)$$

$$y_E(r, t) = \frac{1}{2}\left[1 + \text{erf}\left(\sqrt{\frac{7}{12}}\frac{r - r_f^{ad}(t)}{\sqrt{t}}\right)\right], \qquad (32b)$$

where $r_f^{ad} = (3Qt)^{1/3}$ is the front position in case of nonreactive volume conservation and $\text{erf}(\cdot)$ is the error function. Fig. 8 shows a good agreement between the approximate solutions (32) and the numerical solutions of eqn (8) at early times. Equating the expressions (32a) and (32b), we derive the early-time asymptotic front position $r_{f,E}$, which reads (see Appendix B2)

$$r_{f,E}(t) = r_f^{ad} + \sqrt{\frac{12}{7}}\text{erf}^{-1}\left(\frac{\gamma - 1}{\gamma + 1}\right)t^{1/2},$$

$$\bar{r}_{f,E}(\bar{t}) = r_f^{ad}\bar{\ell} + \sqrt{\frac{12}{7}}\text{erf}^{-1}\left(\frac{\gamma - 1}{\gamma + 1}\right)\sqrt{\bar{D}\bar{t}}. \qquad (33)$$

Notice that, for $\gamma = 1$, the front position is governed by volume conservation only, while for $\gamma \neq 1$ a subleading correction term proportional to $t^{1/2}$ appears. By using eqn (32), we derive the early-time production rate $R_E = x_E^2 y_E$, which reads

$$R_E(r, t) = \frac{\gamma^2}{4}g^2\left(1 - \frac{g}{2}\right), \quad g = 1 - \text{erf}\left(\sqrt{\frac{7}{12}}\frac{r - r_f^{ad}}{\sqrt{t}}\right). \quad (34)$$
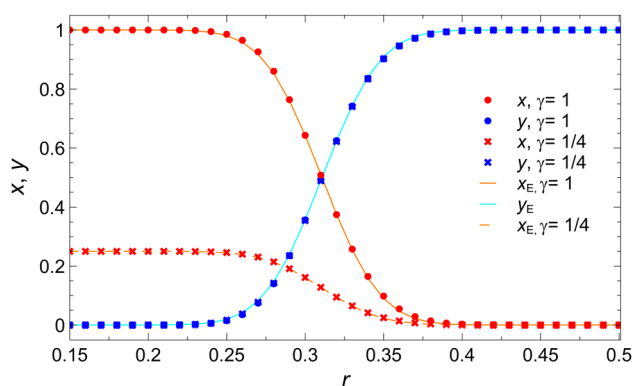
Fig. 8 Concentration profiles for spherical fronts at $t = 10^{-3}$ for $Q = 10$ and $\gamma = 1$. The solid lines represent the approximated solutions (32a) and (32b), and the symbols the numerical solutions of eqn (8).

The position r_E^{max} where the maximum of R_E is located is found by imposing $dR_E/dr = 0$, which implies $g = 4/3$, or explicitly

$$r_E^{max}(t) = r_f^{ad}(t) + \sqrt{\frac{12}{7}}\text{erf}^{-1}(-1/3)t^{1/2},$$

$$\bar{r}_E^{max}(\bar{t}) = r_f^{ad}\bar{\ell} + \sqrt{\frac{12}{7}}\text{erf}^{-1}(-1/3)\sqrt{\bar{D}\bar{t}}. \qquad (35)$$

Notice that, while the front position for spherical autocatalytic fronts is the same as for spherical A + B → C fronts,[28] this is not the case for the position of the maximum production rate, since the latter has a cubic form in the considered autocatalytic reaction. The maximum value R_E^{max} of the early-time production rate is constant, as for the polar case, namely

$$R_E^{max}(t) = \frac{4\gamma^2}{27}, \quad \bar{R}_E^{max}(\bar{t}) = \frac{4k\bar{y}_0^3\gamma^2}{27}. \qquad (36)$$

In Appendix B2, we derive that the front width, defined as the full width at half height of R_E reads

$$w_E(t) = \sqrt{\frac{12}{7}}\left[\text{erf}^{-1}\left(\frac{1}{3}\right) - \text{erf}^{-1}\left(\frac{1 - 2\sqrt{3}}{3}\right)\right]t^{1/2}$$

$$\simeq 1.64t^{1/2},$$

$$\bar{w}_E(\bar{t}) \simeq 1.64\sqrt{\bar{D}\bar{t}}. \qquad (37)$$

Finally, the early-time total amount $n_{X,E}$ of autocatalyst is (see Appendix D)

$$n_{x,E}(t) = 4\pi Q\gamma t, \quad \bar{n}_{x,E}(\bar{t}) = \bar{x}_0\bar{V}, \qquad (38)$$

where we used eqn (9).

B. Long-time regime

In the long-time limit of the spherical fronts dynamics, we can use the same argument of Appendix C and Section IIIA2. In fact, here the term proportional to the flow rate Q decreases as r^{-2}, thus faster than in the polar case. Hence, at long times, the concentration of the reactant Y in the spherical system, solution of eqn (8), can also be described by the cubic eqn (20) with constant c. The resulting concentration profiles are those seen in Fig. 3. Thus, we retrieve the same long time values of observables as in Section IIIA2, except for the total amount of catalytic species, whose long-time limit is derived in Appendix D and reads

$$n_{x,A}(t) \simeq \frac{\sqrt{2\pi}}{3}t^3 \simeq 1.48t^3, \quad \bar{n}_{x,A}(\bar{t}) \simeq 1.48\bar{y}_0\left(\frac{\bar{D}}{\bar{\tau}}\right)^{3/2}\bar{t}^3. \quad (39)$$

The temporal evolution of the front position, the maximum production rate, the front width and the total amount of autocatalyst are shown in Fig. 9.

C. Transition time

To obtain the transition time between the early and the long time regime in spherical geometry, we equate the right hand-side terms of eqn (33) and (23), since the long-time solution for the spherical system is the same as that for polar geometry. For simplicity, in the calculation we only consider the volume conservation term, so
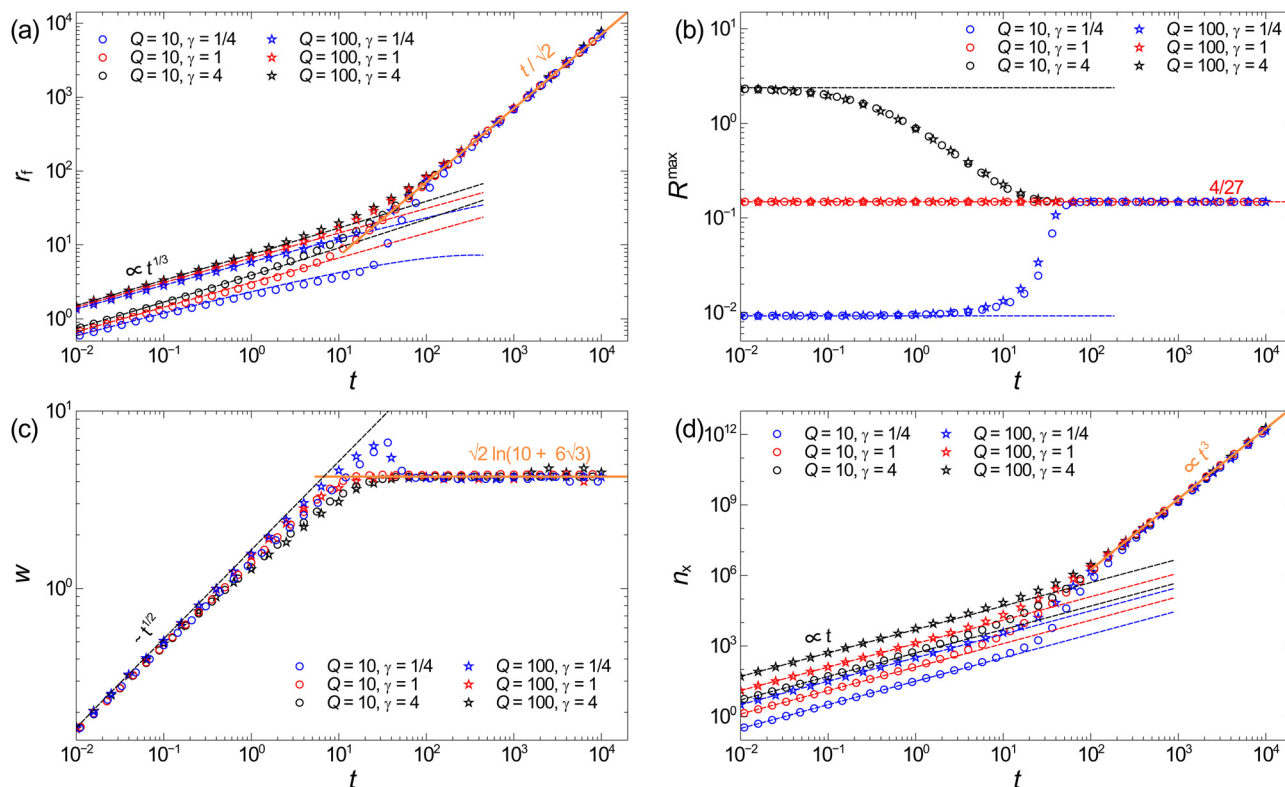
This journal is © the Owner Societies 2023

Phys. Chem. Chem. Phys., 2023, **25**, 10604–10619 | **10611**

Fig. 9 Temporal evolution of the observables for spherical fronts. (a) Front position. The dashed lines represent the $\sim(3Qt)^{1/3}$ trend given by eqn (33), while the solid line represents eqn (23) with slope $t/\sqrt{2}$. (b) Maximum production rate. The dashed lines represent $4\gamma^2/27$, eqn (36), which for $\gamma = 1$ is equal to the long-time asymptotic value 4/27 given by eqn (24). (c) Front width. The dashed line represents eqn (37), while the solid line represents eqn (25). (d) Total amount of the autocatalytic species. The dashed lines represent the early-time behavior (38), while the solid line represents eqn (39).

that we require $(3Qt_{SPH}^*)^{1/3} = t_{SPH}^*/\sqrt{2}$, from which we obtain

$$t_{SPH}^* \simeq 2.91Q^{1/2}, \quad \tilde{t}_{SPH}^* = 2.91\sqrt{\frac{Q\tau^{3/2}}{4\pi D^{3/2}}}. \tag{40}$$

By comparing this equation with the transition timescale in polar geometry (28), we observe that, for a given flow rate $Q > 1$, the transition to RD fronts occurs earlier in spherical than in polar geometry. This is due to the faster decay of the advective term in the spherical geometry.
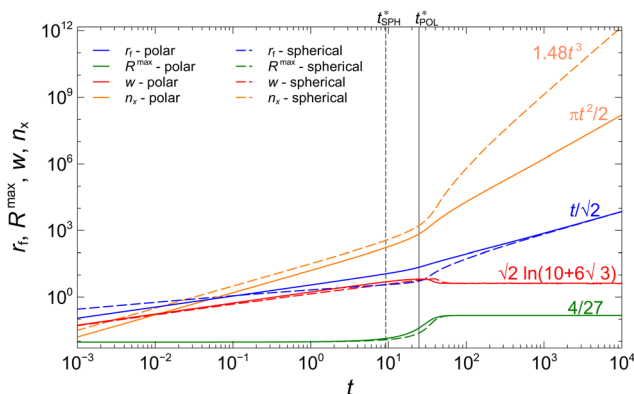

Fig. 10 Temporal evolution of r_f, R^{max}, w and n_x for $Q = 10$ and $\gamma = 1/4$ in radial and spherical geometries.

V. Effect of geometry

Fig. 10 compares the temporal evolution of the characteristic observables of RDA autocatalytic fronts in polar and spherical geometries and provides a visual comparison of the impact of geometry on the system. We observe that, at early times, the front position behaves differently in the two geometries as a consequence of volume conservation. While the temporal scaling of the front width is the same in polar and spherical geometries, its exact value depends on the geometry, although the difference in the multiplicative factors is small. In the long-time regime, the front's position and shape do not depend on the geometry. Both geometries exhibit more efficient production rates of X than the rectilinear geometry, since here the contact area between X and Y increases as the front progresses in the radial direction. However, because the polar geometry describes a confined axisymmetric system, the production of X in such a geometry is less efficient than in the spherical geometry. The difference between the amount of X in polar and spherical geometry is therefore very large at long-times. As an example, in Fig. 10, we observe that, at $t = 10^4$, n_x in the spherical system is approximately 10^4 times larger than in the polar geometry.

VI. Conclusions

In this work, we have investigated the impact of radial advection on cubic autocatalytic fronts. To this end, we have

10612 | *Phys. Chem. Chem. Phys.*, 2023, **25**, 10604–10619

This journal is © the Owner Societies 2023

conducted analytical and numerical analyses of RDA fronts developing when the autocatalytic species X is injected radially into the reactant Y at a constant flow rate in polar and spherical geometries. We have shown that the dynamics of the fronts, which is characterized in terms of the temporal evolution of their position and width, as well as by the maximum of the production rate, exhibits two distinct temporal regimes. At early times, the dynamics is dominated by transport, with advection being the most important process. The early-time dynamics of autocatalytic RDA fronts exhibits important similarities with that of A + B → C fronts, in both polar[26,27,31] and spherical[28] geometries. Indeed, in this regime the total amount of mixing is small, and the governing PDEs can be conveniently approximated by neglecting the reaction term. Thus, at early times, the evolution of the front position is independent of the specific reaction, and it is only determined by volume conservation. For autocatalytic RDA fronts, the maximum production rate and the front width have the same early-time temporal scalings as the A + B → C counterparts. However, the exact shape of the front depends on the specific kinetics, since the production rate is defined as $\bar{R} = \bar{k}\bar{x}\bar{y}$ for bimolecular reaction and as $\bar{R} = \bar{k}\bar{x}^2\bar{y}$ for the cubic autocatalytic reactions considered here.

The long-time dynamics is dominated by the autocatalytic reaction and the dynamics evolves to that of a rectilinear RD front with constant shape and speed with $\gamma = 1$. In particular, advection plays no role in the long-time asymptotic dynamics and we retrieve the same results as for rectilinear RD autocatalytic fronts. While it does not impact the front characteristic observables, geometry still plays an important role for the production of X. Indeed, while in rectilinear geometry the total amount of X grows linearly with time, the increasing volume occupied by the front in radial geometries makes the production of X more efficient. As a consequence, we observe a quadratic and a cubic temporal growth of n_x in polar and spherical geometries, respectively. We remark that the long-time RDA front dynamics of autocatalytic fronts differs significantly from that of RDA bimolecular fronts. In fact, while the long-time dynamics of A + B → C fronts depends on the local balance of the reactants' fluxes, which give rise to diffusive motion in polar[26] and stationarity in spherical[28] geometry, the long-time dynamics of autocatalytic fronts is governed by the autocatalytic reaction and diffusion. Thus, at long times, autocatalytic fronts move faster than A + B → C fronts.

The analytical predictions presented in this work have found good agreement with numerical results and, for polar fronts, with experimental observations made with the chlorite–tetrathionate reaction. This work sheds new light on the properties of autocatalytic fronts in non-uniform advective fields and it may serve as a basis for future studies of the dynamics of RDA in more complex flow fields.

Conflicts of interest

There are no conflicts to declare.

Appendices

Appendix A. Polar decoupled model

We discuss here how to decouple the PDEs (4). To this end, we consider the conservative component $z = x + y$. By summing eqn (4a) and (4b) and performing the change of variable $\eta = r^2/4t$ we obtain

$$\partial_\eta^2 z(\eta) + \left(1 + \frac{1 - Q/2}{\eta}\right)\partial_\eta z(\eta) = 0. \qquad \text{(A1)}$$

The boundary conditions are $z(\eta = 0) = \gamma$ and $z(\eta \to \infty) = 1$. The solution to eqn (A1) that satisfies the boundary conditions reads

$$z(\eta) = \begin{cases} 1 + (\gamma - 1)\mathcal{Q}(Q/2, \eta) & Q > 0, \\ 1 & Q = 0, \ \gamma = 1. \end{cases} \qquad \text{(A2)}$$

For the purely diffusive system ($Q = 0$), eqn (A1) only admits the solution $z = 1$ if $\gamma = 1$, while no solution satisfying the boundary conditions is found when $\gamma \neq 1$. In the diffusive-advective system, eqn (A2) reduces to $z = 1$ if $\gamma = 1$. Therefore, by using eqn (A2), the production rate reads

$$\begin{aligned} R(r, t) &= x^2(r, t)[z(r, t) - x(r, t)] \\ &= x^2(r, t)\left[1 - x(r, t) + (\gamma - 1)\mathcal{Q}(Q/2, r^2/4t)\right]. \end{aligned} \qquad \text{(A3)}$$

Substituting eqn (A3) into eqn (4a) and by using $y = z - x$, we obtain the uncoupled equation

$$\begin{aligned} \partial_t x(r, t) + \frac{Q - 1}{r}\partial_r x(r, t) &= \partial_r^2 x(r, t) \\ &\quad + x^2(r, t)\left[1 - x(r, t) + (\gamma - 1)\mathcal{Q}(Q/2, r^2/4t)\right]. \end{aligned} \qquad \text{(A4)}$$

Therefore, for $Q > 0$ the advective-diffusive system governed by the coupled PDEs (4) is conveniently described by eqn (A4). This equivalence also holds for the purely diffusive system when $\gamma = 1$. Solving eqn (A4) instead of eqn (4) implies an important reduction of the computational cost for the numerical computations.

Appendix B. Early-time regime

1 Polar fronts

Due to the limited amount of mixing, at early times we can neglect the reaction term in eqn (4), which thus reduces to

$$\partial_t x + \frac{Q - 1}{r}\partial_r x = \partial_r^2 x \qquad \text{(B1a)}$$

$$\partial_t y + \frac{Q - 1}{r}\partial_r y = \partial_r^2 y. \qquad \text{(B1b)}$$

By using the change of variables $\eta = r^2/4t$, eqn (B1a) reads

$$\mathrm{d}_\eta^2 x + \left(1 + \frac{1 - Q/2}{\eta}\right)\mathrm{d}_\eta x = 0, \qquad \text{(B2)}$$

whose general solution for $Q > 0$ is

This journal is © the Owner Societies 2023

Phys. Chem. Chem. Phys., 2023, **25**, 10604–10619 | **10613**

$$x_E(\eta) = c_1\Gamma(Q/2,\eta) + c_2, \tag{B3}$$

where the index E stands for early-time and the constants c_1 and c_2 are obtained by imposing the boundary conditions $x_E(0) = \gamma$ and $x_E(\infty) = 0$. By recalling that $\Gamma(Q/2,\infty) = 0$ and $\Gamma(Q/2,0) = \Gamma(Q/2)$, we obtain

$$x_E(r,t) = \gamma\frac{\Gamma(Q/2,\eta)}{\Gamma(Q/2,0)} = \gamma\mathcal{Q}\left(\frac{Q}{2},\frac{r^2}{4t}\right). \tag{B4}$$

Analogously, solving eqn (B1b) with the boundary conditions $y_E(0) = 0$ and $y_E(\infty) = 1$, we obtain

$$y_E(r,t) = 1 - \mathcal{Q}\left(\frac{Q}{2},\frac{r^2}{4t}\right) = 1 - \frac{x_E(r,t)}{\gamma}. \tag{B5}$$

The early-time production rate R_E is defined as

$$R_E(r,t) = x_E^2(r,t)y_E(r,t). \tag{B6}$$

By substituting eqn (B4) and (B5) into this expression, we obtain

$$R_E(r,t) = \gamma^2\mathcal{Q}^2\left(\frac{Q}{2},\frac{r^2}{4t}\right)\left[1 - \mathcal{Q}\left(\frac{Q}{2},\frac{r^2}{4t}\right)\right] \tag{B7}$$

$$= x_E^2(r,t)\left(1 - \frac{x_E(r,t)}{\gamma}\right). \tag{B8}$$

The concentration $x_E^{\max}$ that maximizes the production rate is found by using eqn (B8) and imposing $\mathrm{d}R_E/\mathrm{d}x_E|_{x_E=x_E^{\max}} = 0$. We obtain $x_E^{\max} = 2\gamma/3$. Therefore, the maximum production rate reads

$$R_E^{\max} = (x_E^{\max})^2\left(1 - x_E^{\max}/\gamma\right) = \frac{4\gamma^2}{27}. \tag{B9}$$

The position $r_E^{\max}$ where the production rate is maximum, *i.e.* $\partial R_E/\partial_r|_{r=r_E^{\max}} = 0$, reads

$$r_E^{\max}(t) = 2\sqrt{\mathcal{Q}^{-1}\left(\frac{Q}{2},\frac{2}{3}\right)t} \underset{Q\gg1}{=} \sqrt{2Qt}. \tag{B10}$$

The early-time front width w_E is defined here as the width at half-height of the production rate R_E. We first look for the values of x_E such that the right side of eqn (B8) equals $R_E^{\max}/2$. Hence, by using eqn (B9)

$$\frac{2\gamma^2}{27} = x_E^2\left(1 - \frac{x_E}{\gamma}\right), \tag{B11}$$

whose positive solutions are

$$x_{E,1} = \frac{\gamma}{3}, \quad x_{E,2} = \frac{\gamma}{3}(1 + \sqrt{3}). \tag{B12}$$

Hence, by substituting these expressions into eqn (B4) and solving for r, we find the radial positions r_1 and r_2 where the production rate equals $R_E^{\max}/2$, namely

$$r_1(t) = 2\sqrt{\mathcal{Q}^{-1}\left(\frac{Q}{2},\frac{1}{3}\right)t}, \tag{B13}$$

$$r_2(t) = 2\sqrt{\mathcal{Q}^{-1}\left(\frac{Q}{2},\frac{1+\sqrt{3}}{3}\right)t}. \tag{B14}$$
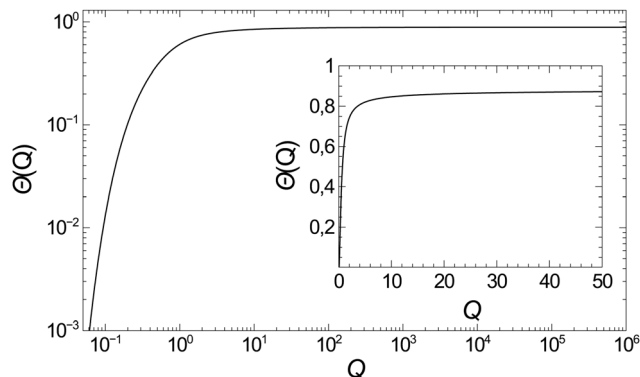

Fig. 11 Coefficient Θ as a function of the flow rate in log–log (main) and linear scale (inset).

The front width is thus

$$w_E(t) = r_1(t) - r_2(t) = 2\Theta(Q)\sqrt{t}, \tag{B15}$$

where the function

$$\Theta(Q) = \sqrt{\mathcal{Q}^{-1}\left(\frac{Q}{2},\frac{1}{3}\right)} - \sqrt{\mathcal{Q}^{-1}\left(\frac{Q}{2},\frac{1+\sqrt{3}}{3}\right)}. \tag{B16}$$

is shown in Fig. 11. Eqn (B16) simplifies a lot in the limit of large flow rate, *i.e.* for $Q \gg 1$. Indeed, by using the equivalence

$$\mathcal{Q}^{-1}(x,a) \simeq x + \sqrt{2x}\,\mathrm{erfc}^{-1}(2a), \quad x \gg 1 \tag{B17}$$

where $\mathrm{erfc}^{-1}(\cdot)$ is the inverse of the complementary error function and by substituting this expression into eqn (B16) we obtain

$$\Theta(Q) = \sqrt{\frac{Q}{2}}\left[\sqrt{1 + \frac{2\mathrm{erfc}^{-1}\left(\frac{2}{3}\right)}{\sqrt{Q}}}\right.$$

$$\left. - \sqrt{1 + \frac{2\mathrm{erfc}^{-1}\left(\frac{2+2\sqrt{3}}{3}\right)}{\sqrt{Q}}}\right]. \tag{B18}$$

In the limit $Q \gg 1$, by using the Taylor expansion $(1+\varepsilon)^{1/2} \simeq 1 + \varepsilon/2$ for $\varepsilon \ll 1$, we finally obtain

$$\Theta \simeq \frac{1}{\sqrt{2}}\left[\mathrm{erfc}^{-1}\left(\frac{2}{3}\right) - \mathrm{erfc}^{-1}\left(\frac{2+2\sqrt{3}}{3}\right)\right] \simeq 0.89. \tag{B19}$$

2 Spherical fronts

To derive the solutions for the early-time dynamics of spherical autocatalytic fronts, we follow the derivation in ref. 28, which is reported here for the reader's convenience. In analogy to the polar front case, we assume that the amount of mixing at early times is small. Since at early times the dynamics is mainly driven by diffusion and advection, we assume that the concentrations of X and Y can be written in the form $x(r,t) = x([r - r_f^{ad}(t)]/t^\alpha)$ and $y(r,t) = y([r - r_f^{ad}(t)]/t^\alpha)$, where $r_f^{ad} = (3Qt)^{1/3}$ is

the position of a front moving by volume conservation only and α is a coefficient to be determined. By substituting the ansatz into eqn (8a), we get

$$\frac{d^2 x}{d\zeta^2} + \left[\alpha \zeta t^{2\alpha-1} + \frac{2t^\alpha}{r_f^{ad} + \zeta t^\alpha} + \frac{Qt^\alpha}{(r_f^{ad})^2} - \frac{Qt^\alpha}{(r_f^{ad} + \zeta t^\alpha)^2} \right] \frac{dx}{d\zeta} + t^{2\alpha} R = 0,$$
(B20)

where $\zeta = (r - r_f^{ad})/t^\alpha$. We consider the limit $t \to 0$ for fixed ζ as in ref. 28. If $\alpha < 1/2$, the first term in the square brackets of eqn (B20) diverges and leads to a nonphysical solution. For $\alpha \geq 1/2$, in the limit $t \to 0$, the second and fourth terms in the square brackets of eqn (B20) simplify as $r_f^{ad} \gg \zeta t^\alpha$, leading to

$$\frac{d^2 x}{d\zeta^2} + \left[\left(\frac{2}{3} + \alpha \right) \zeta t^{2\alpha-1} + \frac{2t^{\alpha-1/3}}{(3Q)^{1/3}} \right] \frac{dx}{d\zeta} + t^{2\alpha} R = 0.$$
(B21)

If $\alpha > 1/2$ the equation provides again a nonphysical solution in the limit $t \to 0$. Hence, it must be $\alpha = 1/2$, which hinges on diffusion. Thus, considering the leading terms, the previous equation reduces to

$$\frac{d^2 x}{d\zeta^2} + \frac{7\zeta}{6} \frac{dx}{d\zeta} = 0, \quad x(-\infty) = \gamma \; x(\infty) = 0,$$
(B22)

where the boundary conditions are derived from those in Section IIA. By applying the same derivation for Y, starting from eqn (8b), we get

$$\frac{d^2 y}{d\zeta^2} + \frac{7\zeta}{6} \frac{dy}{d\zeta} = 0, \quad y(-\infty) = 0 \quad y(\infty) = 1.$$
(B23)

Eqn (B22) and (B23) describe a simplified problem that conveniently approximates eqn (8) at short time. The solutions of eqn (B22) and (B23) that satisfy the boundary conditions read

$$x_E(r, t) = \frac{\gamma}{2} \left[1 - \text{erf} \left(\sqrt{\frac{7}{12}} \zeta \right) \right]$$
(B24a)

$$y_E(r, t) = \frac{1}{2} \left[1 + \text{erf} \left(\sqrt{\frac{7}{12}} \zeta \right) \right] = 1 - \frac{x_E(r, t)}{\gamma}.$$
(B24b)

Substituting the definition $\zeta = (r - r_f^{ad})/\sqrt{t}$ finally leads to eqn (32).

To obtain the early-time front position $\zeta_{f,E}$, we equate the right-hand sides of eqn (B24) and we obtain

$$\zeta_{f,E} = \sqrt{\frac{12}{7}} \text{erf}^{-1} \left(\frac{\gamma - 1}{\gamma + 1} \right)$$
(B25)

and by using the definition of ζ we finally get eqn (33).

In order to find the width w_E at half-height of R_E, we look for the solutions of $R_E(g) = R_E^{max}/2$, where R_E and g are given by eqn (34). Notice that, since $R_E = x_E^2(1 - x_E/\gamma)$, as in the polar case, its maximum, R_E^{max} has the same value, hence $R_E^{max} = 4\gamma^2/27$. Hence, we need to solve again eqn (B11). By substituting its solutions (B12) into eqn (B24) and by solving for r, we obtain

$$r_1 = r_f^{ad}(t) + \sqrt{\frac{12}{7}} \text{erf}^{-1} \left(\frac{1}{3} \right) t^{1/2}$$
(B26)

$$r_2 = r_f^{ad}(t) + \sqrt{\frac{12}{7}} \text{erf}^{-1} \left(\frac{1 - 2\sqrt{3}}{3} \right) t^{1/2}.$$
(B27)

The front width is therefore

$$w_E(t) = r_1(t) - r_2(t) \simeq 1.64 t^{1/2},$$
(B28)

which coincide with eqn (37).

Appendix C. Long-time regime

1. Polar fronts

For the derivation of the long-time dynamics of polar fronts, we use the change of variables $\xi = r - r_{f,A}(t)$, where $r_{f,A}$ is the long-time front position. Thus, eqn (4b) reads

$$d_\xi^2 y_A + \left[c(t) - \frac{Q - 1}{\xi + r_{f,A}} \right] d_\xi y_A - x_A^2 y_A = 0,$$
(C1)

where $c(t) = dr_f(t)/dt$ is the front speed and we have used the index A to refer to the asymptotic long-time regime. We introduce here an assumption, which is verified *a posteriori* through numerical computations. We assume that, in the long-time limit, the front moves with a constant velocity $c(t \to \infty) = c$, *i.e.* the front position scales as $r_{f,A}(t) \sim ct$. Therefore, for $t \to \infty$, the condition $c \gg (Q - 1)/(\xi + r_{f,A})$ holds, provided that $|\xi| \gg -r_{f,A}$, *i.e.* for $r \gg 0$, where the gradients of x and y vanish, and either of the two concentrations vanish as well. Only in the proximity of the front, *i.e.* for $|\xi| \sim 0$, each term is significantly different from zero, so we consider that $|\xi|$ is never large. Thus, we can neglect the second term in the square brackets in eqn (C1), which then reads

$$d_\xi^2 y_A + c d_\xi y_A - x_A^2 y_A = 0.$$
(C2)

We recall that if the initial concentrations of X and Y are equal, then $z = x + y = 1$. Fig. 4 shows that, for $\gamma \neq 1$, in the long-time limit the concentration of x increases or decreases over a distance r_0 to reach the value of 1. This distance is independent of γ and, for $Q \gg 1$, it increases as $r_0 \sim Q^{1/3}$. Because the front is located at a distance $r_{f,A} \gg r_0$, the impact of γ on the front dynamics in this regime can be neglected. Thus, we conclude that $z_A = x_A + y_A = 1$. Hence, by substituting this expression into eqn (C2), we get the cubic Fisher equation

$$d_\xi^2 y_A + c d_\xi y_A - (1 - y_A)^2 y_A = 0,$$
(C3)

as for RD autocatalytic fronts with no advection. Its solution satisfying the boundary conditions $y_A(-\infty) = 0$ and $y_A(\infty) = 1$ is eqn (21).[25] Notice that the solution for x_A is valid for $r > r_0$.

The long-time production rate is obtained by substituting eqn (22) and (21) into $R_A = x_A^2 y_A$, leading to

$$R_A(r, t) = \frac{\exp \left[-2 \dfrac{r - r_{f,A}(t)}{\sqrt{2}} \right]}{\left(1 + \exp \left[-\dfrac{r - r_{f,A}(t)}{\sqrt{2}} \right] \right)^3}.$$
(C4)

This journal is © the Owner Societies 2023

Phys. Chem. Chem. Phys., 2023, **25**, 10604–10619 | **10615**

The maximum value of R_A is $R_A^{max} = 4/27$ and it is located at

$$r_{max,A}(t) = r_{f,A}(t) - \sqrt{2}\ln(2) = \frac{t}{\sqrt{2}} - \sqrt{2}\ln(2). \qquad (C5)$$

Thus, the distance between $r_{f,A}$ and $r_{max,A}$ is constant and it becomes negligible for $t \to \infty$.

The width at half-height of R_A is obtained by imposing $R_A(r,t) = R_A^{max}/2$. By using eqn (24) and (C4), we obtain

$$\frac{\chi^2}{(1+\chi)^3} = \frac{2}{27}, \qquad (C6)$$

where $\chi = \exp[-(r - r_{f,A})/\sqrt{2}]$. Solving eqn (C6) provides the two positive solutions $\chi_1 = 1/2$ and $\chi_2 = 5 + 3\sqrt{3}$. By substituting these solutions into the definition of χ, we obtain $r_1 = r_{f,A} + \sqrt{2}\ln(2)$ and $r_2 = r_{f,A} - \sqrt{2}\ln(5 + 3\sqrt{3})$. Thus, the width reads

$$w_A(t) = r_1(t) - r_2(t) = \sqrt{2}\ln(10 + 6\sqrt{3}). \qquad (C7)$$

Finally, for spherical fronts, we apply again the change of variables $\xi = r - r_{f,A}(t)$ into eqn (8b), which reduces to

$$d_\xi^2 y_A + \left[c(t) - \frac{Q}{(\xi + r_{f,A})^2} + \frac{2}{\xi + r_{f,A}} \right] d_\xi y_A - x_A^2 y_A = 0. \quad (C8)$$

By using the ansatz $c(t) = c$ constant, and by taking the limit $t \to \infty$, we obtain again eqn (C2). Hence, in the long-time regime the dynamics of autocatalytic fronts is independent of the geometry and advection. Thus, for spherical fronts, we obtain the same long-time behavior as described above for polar fronts.

2. Spherical fronts

By using the change of variables $\xi = r - r_{f,A}(t)$, in the long-time regime eqn (8) reads

$$d_\xi^2 y_A + \left[c(t) - \frac{Q}{(\xi + r_{f,A})^2} + \frac{2}{\xi + r_{f,A}} \right] d_\xi y_A - x_A^2 y_A = 0. \quad (C9)$$

In the previous section, we have shown that $Q/(\xi + r_{f,A})$ vanishes in the long time limit. This is of course also true for $Q/(\xi + r_{f,A})^2$. Hence, once again we can neglect the second and the third term in the square brackets and eqn (C9) reduces to eqn (C2). Therefore, the results derived above for polar fronts also hold for the long-time dynamics of spherical fronts.

Appendix D. Total amount of catalytic species

1. Polar geometry

Here we derive the early-time and the long-time limits of the total amount of catalytic species in polar geometry. To this end, we will follow the methodology described in ref. 26 for polar and ref. 28 for spherical A + B → C fronts. First, we multiply

eqn (4a) by $2\pi hr$ and we integrate over the radial coordinate

$$\frac{d}{dt}\int_0^\infty 2\pi hr x(r,t)dr = -2\pi h(Q-1)\int_0^\infty \partial_r x(r,t)dr + 2\pi h$$
$$\times \int_0^\infty r\partial_r^2 x(r,t)dr + 2\pi h\int_0^\infty rR(r,t)dr = \frac{dn_x}{dt} \qquad (D1)$$

Notice that the first integral on the left hand-side is the total amount of X, as defined in eqn (11a). We calculate each integral term separately. Because of the boundary conditions $x(0,t) = \gamma$ and $x(\infty,t) = 0$, we obtain

$$\int_0^\infty \partial_r x(r,t)dr = x(r,t)|_0^\infty = -\gamma. \qquad (D2)$$

By performing integration by parts and by assuming that the gradient of x decays faster than $1/r$ for $r \to \infty$, we obtain

$$\int_0^\infty r\partial_r^2 x dr = \gamma. \qquad (D3)$$

Thus, by substituting eqn (D2) and (D3) into eqn (D1), we get

$$\frac{dn_x(t)}{dt} = 2\pi h\gamma Q + 2\pi h\int_0^\infty rR(r,t)dr. \qquad (D4)$$

Next, we assume that the production rate $R(r,t)$ is a well-peaked function around r_f, that can be written in the form

$$R(r,t) = R^{max}\Phi\left(\frac{r - r_f(t)}{w(t)}\right), \qquad (D5)$$

where Φ is a well-peaked function around zero. Thus,

$$\int_0^\infty rR(r,t)dt = \int_0^\infty rR^{max}\Phi\left(\frac{r - r_f(t)}{w(t)}\right)dr. \qquad (D6)$$

By using the change of variable $\varphi = (r - r_f)/w$ into eqn (D6), we obtain

$$\int_0^\infty rR(r,t)dt = wR^{max}\int_{-r_f/w}^\infty (w\varphi + r_f)\Phi(\varphi)d\varphi. \qquad (D7)$$

Notice that $r_f/w \gg 1$ in both the early and the long-time regime. Indeed, at early times r_f, $w \sim t^{1/2}$, so their ratio is time-independent. It grows as $Q^{1/2}$ and depends weakly on γ. At long times, $r_f \sim t$ and w is constant. Thus, and since the function $\Phi(\varphi)$ vanishes fast for $|\varphi| > 0$, we can replace the limit of integration $-r_f/w$ in eqn (D7) by $-\infty$. Moreover, we introduce the n-th order moments μ_n of Φ, defined as

$$\mu_n = \int_{-\infty}^\infty \varphi^n\Phi(\varphi)d\varphi, \qquad (D8)$$

so that eqn (D7) reduces to

$$\int_0^\infty rR(r,t)dt = \mu_0 wR^{max}r_f(t) + \mu_1 w^2 R^{max}. \qquad (D9)$$

By substituting eqn (D9) into eqn (D4), we get

$$\frac{dn_x(t)}{dt} = 2\pi h[\gamma Q + \mu_0 wR^{max}r_f(t) + \mu_1 w^2 R^{max}]. \qquad (D10)$$

In order to derive the early- and the long-time behavior of $n_x(t)$, we use the corresponding expressions of r_f, w and R^{max} that we derived in Section III. At early times, $r_{f,E} \propto t^{1/2}$, $w_E \propto t^{1/2}$ and $R_E^{max} = 4\gamma^2/27$. Thus, by taking only the leading term in eqn (D4) for $t \to 0$, we get

$$\frac{dn_{x,E}(t)}{dt} = 2\pi h Q \gamma, \qquad (D11)$$

and temporal integration provides

$$n_{x,E}(t) = 2\pi h Q \gamma t. \qquad (D12)$$

In the long-time limit, $r_{f,A} \sim t/\sqrt{2}$, while R_A^{max} and w_A are constant. Hence, by substituting this expressions and eqn (D9) into eqn (D4) and by taking only the leading term for $t \to \infty$, we get

$$\frac{dn_{x,A}(t)}{dt} = \mu_0 \frac{2\pi h w_A R_A^{max}}{\sqrt{2}} t. \qquad (D13)$$

Finally, we determine the value of μ_0. By definition,

$$\mu_0 = \int_{-\infty}^{\infty} \Phi(\varphi) d\varphi = \int_{-\infty}^{\infty} R(\varphi)/R_A^{max} d\varphi, \qquad (D14)$$

where we have used eqn (D5). By using the definition $\varphi = (r - r_f)/w_A$ into eqn (C4), we obtain

$$\mu_0 = \frac{1}{R_A^{max}} \int_{-\infty}^{\infty} \frac{\exp\left(-\frac{2w_A \varphi}{\sqrt{2}}\right)}{\left[1 + \exp\left(-\frac{w_A \varphi}{\sqrt{2}}\right)\right]^3} d\varphi. \qquad (D15)$$

By applying the change of variable $\varphi' = w_A \varphi/\sqrt{2}$, the previous equation reduces to

$$\mu_0 = \frac{\sqrt{2}}{w_A R_A^{max}} \int_{-\infty}^{\infty} \frac{\exp(-2\varphi')}{[1 + \exp(-\varphi')]^3} d\varphi' = \frac{\sqrt{2}}{2w_A R_A^{max}}. \qquad (D16)$$

Thus, by substituting the latter expression into eqn (D13) and by performing time integration, we obtain

$$n_{x,A}(t) = \frac{\pi h}{2} t^2. \qquad (D17)$$

2. Spherical geometry

Here we derive the early-time and the long-time limits of the total amount of autocatalyst in spherical geometry. We proceed in an analogous way as in the previous section. First, we multiply eqn (8a) by $4\pi r^2$ and we integrate over the radial coordinate

$$\frac{d}{dt} \int_0^\infty 4\pi r^2 x(r,t) dr = -4\pi Q \int_0^\infty \partial_r x(r,t) dr$$

$$+ 4\pi \int_0^\infty r^2 \partial_r^2 x(r,t) dr + 8\pi \int_0^\infty r \partial_r x(r,t) dr$$

$$+ 4\pi \int_0^\infty r^2 R(r,t) dr = \frac{dn_x}{dt}. \qquad (D18)$$

Again, the first integral on the left hand-side is the total amount

of autocatalyst, as defined in eqn (11b). We calculate each integral term separately. By performing integration by parts, and by assuming that the gradient of x vanishes faster than $1/r^2$ for $r \to \infty$, the second integral on the right hand-side of eqn (D18) reduces to

$$\int_0^\infty r^2 \partial_r^2 x(r,t) dr = r^2 \partial_r x(r,t) \big|_0^\infty - 2 \int_0^\infty r \partial_r x dr$$

$$= -2 \int_0^\infty r \partial_r x dr \qquad (D19)$$

and it cancels out with the third term on the right-hand side of eqn (D18). To compute the last integral in eqn (D18), we use again the well-peaked approximation (D5) for R. Thus,

$$\int_0^\infty r^2 R(r,t) dt = \int_0^\infty r^2 R^{max} \Phi\left(\frac{r - r_f(t)}{w(t)}\right) dr. \qquad (D20)$$

By using the change of variable $\varphi = (r - r_f)/w$ into eqn (D20), we obtain

$$\int_0^\infty r^2 R(r,t) dt = w R^{max} \int_{-r_f/w}^{\infty} (w^2 \varphi^2 + r_f^2 + 2w r_f \varphi) \Phi(\varphi) d\varphi. \qquad (D21)$$

We can again extend the lower limit of integration to $-\infty$, since the ratio r_f/w diverges for both $t \to 0$ and $t \to \infty$. Thus, eqn (D21) reduces to

$$\int_0^\infty r^2 R(r,t) dt = \mu_0 R^{max} w(t) r_f^2(t) + 2\mu_1 R^{max} w^2(t) r_f(t)$$

$$+ \mu_2 R^{max} w^3(t), \qquad (D22)$$

where μ_0, μ_1 and μ_2 are defined as in eqn (D8). By substituting eqn (D2), (D19) and (D22) into eqn (D18), we get that the growth rate of n_x is

$$\frac{dn_x(t)}{dt} = 4\pi \big[Q\gamma + \mu_0 R^{max} w(t) r_f^2(t)$$

$$+ 2\mu_1 R^{max} w^2(t) r_f(t) + \mu_2 R^{max} w^3(t) \big]. \qquad (D23)$$

In order to derive the early-time and the long-time behavior of $n_x(t)$, we use the corresponding expressions of r_f, w and R^{max}. At early times (see Section IV) $r_{f,E} \propto t^{1/3}$, $w_E \sim t^{1/2}$ and $R_E^{max} = 4\gamma^2/27$. Thus, by taking only the leading term in eqn (D23) for $t \to 0$, we get

$$\frac{dn_{x,E}(t)}{dt} = 4\pi Q \gamma. \qquad (D24)$$

Integration over time provides eqn (38). In the long-time limit, see Section IIIA2, $r_{f,A} = t/\sqrt{2}$, $w_A = \sqrt{2}\ln(10 + 6\sqrt{3})$ and $R_A^{max} = 4/27$. By substituting these expressions into eqn (D23) and by neglecting the subleading terms for $t \to \infty$, we get

$$\frac{dn_{x,A}(t)}{dt} = 2\pi \mu_0 R_A^{max} w_A t^2. \qquad (D25)$$

By substituting eqn (D16) and by performing time integration,

This journal is © the Owner Societies 2023

Phys. Chem. Chem. Phys., 2023, **25**, 10604–10619 | **10617**

we finally get

$$n_{x,\mathrm{A}}(t) \simeq \frac{\sqrt{2}\pi}{3}t^3. \qquad \text{(D26)}$$

Acknowledgements

References

1 P. J. Ortoleva, *Geochemical self-organization*, Oxford University Press, Oxford, 1994.

2 J. D. Murray, *Mathematical biology*, Springer Verlag, Berlin, 2003.

3 J. H. Seinfeld and S. N. Pandis, *Atmospheric Chemistry and Physics*, John Wiley & Sons Inc, New York, 2nd edn, 2006.

4 I. Mastromatteo, B. Toth and J. P. Bouchaud, Anomalous impact in reaction–diffusion financial models, *Phys. Rev. Lett.*, 2014, **113**(26), 268701.

5 S. Fornari, A. Schäfer, M. Jucker, A. Goriely and E. Kuhl, Prionlike spreading of Alzheimer's disease within the brain's connectome, *J. R. Soc., Interface*, 2019, **16**(159), 20190356.

6 S. K. Scott and K. Showalter, Simple and complex propagating reaction–diffusion fronts, *J. Phys. Chem.*, 1992, **96**(22), 8702–8711.

7 J. A. Pojman, Traveling fronts of methacrylic acid polymerization, *J. Am. Chem. Soc.*, 1991, **113**(16), 6284–6286.

8 R. A. Fisher, The wave of advance of advantageous genes, *Ann. Eugen.*, 1937, **7**(4), 355–369.

9 A. N. Kolmogorov, I. G. Petrovsky and N. S. Piskunov, Investigation of the equation of diffusion combined with increasing of the substance and its application to a biology problem, *Bull. Moscow State Univ. Ser. A: Math. Mech.*, 1937, **1**(6), 1–25.

10 J. Billingham and D. J. Needham, The development of travelling waves in quadratic and cubic autocatalysis with unequal diffusion rates. I. Permanent form travelling waves, *Philos. Trans. R. Soc., A*, 1991, **334**(1633), 1–24.

11 A. Hanna, A. Saul and K. Showalter, Detailed studies of propagating fronts in the iodate oxidation of arsenous acid, *J. Am. Chem. Soc.*, 1982, **104**(14), 3838–3844.

12 D. Horváth, V. Petrov, S. K. Scott and K. Showalter, Instabilities in propagating reaction–diffusion fronts, *J. Chem. Phys.*, 1993, **98**(8), 6332–6343.

13 D. Horváth and K. Showalter, Instabilities in propagating reaction–diffusion fronts of the iodate-arsenous acid reaction, *J. Chem. Phys.*, 1995, **102**(6), 2471–2478.

14 D. Horváth and Á. Tóth, Diffusion-driven front instabilities in the chlorite–tetrathionate reaction, *J. Chem. Phys.*, 1998, **108**(4), 1447–1451.

15 A. De Wit, Chemo-hydrodynamic patterns and instabilities, *Annu. Rev. Fluid Mech.*, 2020, **52**, 531–555.

16 A. B. Rovinsky and M. Menzinger, *Phys. Rev. Lett.*, 1992, **69**, 1193.

17 P. Andresen, M. Bache, E. Mosekilde, G. Dewel and P. Borckmans, Stationary space-periodic structures with equal diffusion coefficients, *Phys. Rev. E: Stat. Phys., Plasmas, Fluids, Relat. Interdiscip. Top.*, 1999, **60**, 297.

18 C. R. Nugent, W. M. Quarles and T. H. Solomon, Experimental Studies of Pattern Formation in a Reaction-Advection-Diffusion System, *Phys. Rev. Lett.*, 2004, **93**, 218301.

19 C. Rana and A. De Wit, Reaction-driven oscillating viscous fingering, *Chaos*, 2019, **29**, 043115.

20 M. A. Budroni, L. Lemaigre, D. M. Escala and A. De Wit, Buoyancy-Driven Chemohydrodynamic Patterns in A + B → Oscillator Two-Layer Stratifications, *Langmuir*, 2023, **29**, 997.

21 B. F. Edwards, *Phys. Rev. Lett.*, 2002, **89**, 104501.

22 M. Leconte, J. Martin, N. Rakotomalala and D. Salin, Pattern of reaction diffusion fronts in laminar flows, *Phys. Rev. Lett.*, 2003, **90**(12), 128302.

23 M. Abel, A. Celani, D. Vergni and A. Vulpiani, Front propagation in laminar flows, *Phys. Rev. E: Stat., Nonlinear, Soft Matter Phys.*, 2001, **64**, 46307.

24 M. Leconte, N. Jarrige, J. Martin, N. Rakotomalala, D. Salin and L. Talon, Taylor's regime of an autocatalytic reaction front in a pulsative periodic flow, *Phys. Fluids*, 2008, **20**(5), 057102.

25 R. A. Milton and S. K. Scott, The dynamics and stability of cubic autocatalytic chemical waves in threedimensional systems, *Proc. R. Soc. A*, 1996, **452**(1945), 391–419.

26 F. Brau, G. Schuszter and A. De Wit, Flow control of A + B → C fronts by radial injection, *Phys. Rev. Lett.*, 2017, **118**(13), 134101.

27 P. M. J. Trevelyan and A. J. Walker, Asymptotic properties of radial A + B → C reaction fronts, *Phys. Rev. E*, 2018, **98**(3), 032118.

28 A. Comolli, A. De Wit and F. Brau, Dynamics of A + B → C reaction fronts under radial advection in three dimensions, *Phys. Rev. E*, 2019, **100**(5), 052213.

29 F. Brau and A. De Wit, Influence of rectilinear vs radial advection on the yield of A + B→ C reaction fronts: A comparison, *J. Chem. Phys.*, 2020, **152**(5), 054716.

30 Á. Tóth, G. Schuszter, N. P. Das, E. Lantos, D. Horváth and A. De Wit, *et al.*, Effects of radial injection and solution thickness on the dynamics of confined A + B → C chemical fronts, *Phys. Chem. Chem. Phys.*, 2020, **22**, 10278–10285, DOI: **10.1039/C9CP06370F**.

31 A. Comolli, A. De Wit and F. Brau, Dynamics of A+ B→ C reaction fronts under radial advection in a Poiseuille flow, *Phys. Rev. E*, 2021, **104**(4), 044206.

32 E. Guilbert, C. Almarcha and E. Villermaux, Chemical reaction for mixing studies, *Phys. Rev. Fluids*, 2021, **6**(11), 114501.

33 Y. Stergiou, M. J. B. Hauser, A. Comolli, F. Brau, A. De Wit and G. Schuszter, *et al.*, Effects of gravity modulation on the dynamics of a radial A + B → C reaction front, *Chem. Eng. Sci.*, 2022, **257**, 117703.

34 I. Nagypal and I. R. Epstein, Fluctuations and stirring rate effects in the chlorite-thiosulfate reaction, *J. Phys. Chem.*, 1986, **90**(23), 6285–6292.

35 Á. Tóth, D. Horváth and A. Siska, Velocity of propagation in reaction–diffusion fronts of the chlorite–tetrathionate reaction, *J. Chem. Soc., Faraday Trans.*, 1997, **93**(1), 73–76.

36 R. Tiani, A. De Wit and L. Rongy, Surface tension- and buoyancy-driven flows across horizontally propagating chemical fronts, *Adv. Colloid Interface Sci.*, 2018, **225**, 76–83.

37 F. Haudin, L. A. Riolfo, B. Knaepen, G. M. Homsy and A. De Wit, Experimental study of a buoyancy-driven instability of a miscible horizontal displacement in a Hele-Shaw cell, *Phys. Fluids*, 2014, **26**, 044102.

38 F. W. J. Olver, D. W. Lozier, R. F. Boisvert and C. W. Clark, *NIST Handbook of Mathematical Functions*, Cambridge University Press, 2010.

39 P. Gray and S. K. Scott, *Chemical oscillations and instabilities: non-linear chemical kinetics*, International Series of Monographs on Chemistry, Clarendon Press, Oxford, 1990, vol. 21.

40 P. Gray, S. K. Scott and K. Showalter, The influence of the form of autocatalysis on the speed of chemical waves, *Philos. Trans. R. Soc., A*, 1991, **337**(1646), 249–260.

41 D. Horváth, T. Bánsági Jr and Á. Tóth, Orientation dependent density fingering in an acidity front, *J. Chem. Phys.*, 2002, **117**(9), 4399–4402.

42 J. Yang, A. D'Onofrio, S. Kalliadasis and A. De Wit, Rayleigh–Taylor instability of reaction–diffusion acidity fronts, *J. Chem. Phys.*, 2002, **117**(20), 9395–9408.

43 T. Bánsági Jr, D. Horváth, Á. Tóth, J. Yang, S. Kalliadasis and A. De Wit, Density fingering of an exothermic autocatalytic reaction, *Phys. Rev. E: Stat., Nonlinear, Soft Matter Phys.*, 2003, **68**(5), 055301(R).

44 D. Lima, A. D'Onofrio and A. De Wit, Nonlinear fingering dynamics of reaction–diffusion acidity fronts: Self-similar scaling and influence of differential diffusion, *J. Chem. Phys.*, 2006, **124**(1), 014509.

45 G. Panzarasa, Clocking the Clock: Programmable Acid Autocatalysis in the Chlorite–tetrathionate Reaction, *ChemistrySelect*, 2020, **5**(27), 8074–8077.

46 B. Bohner, G. Schuszter, H. Nakanishi, D. Zámbó, A. Deák and D. Horváth, *et al.*, Self-assembly of charged nanoparticles by an autocatalytic reaction front, *Langmuir*, 2015, **31**(44), 12019–12024.

This journal is © the Owner Societies 2023

Phys. Chem. Chem. Phys., 2023, **25**, 10604–10619 | **10619**